RESEARCH ARTICLE
SOLAR PHYSICS

Earth and Planetary Physics
9: 740–751, 2025
doi: 10.26464/epp2025036

Diagnostics of temperature and blue-shifted velocity using soft X-ray spectra from the Macau Science Satellite-1

JianPing Li[1], Xu Yang[2], Dong Li[1], JinHua Shen[3], Lei Yang[1], Ya Wang[1], LianSheng Li[4], YongQiang Shi[4], and HaiSheng Ji[1,3*]

[1]Key Laboratory of Dark Matter and Space Astronomy, Purple Mountain Observatory, Chinese Academy of Sciences, Nanjing 210023, China;

[2]Big Bear Solar Observatory 40386 N Shore Ln Big Bear, CA 92314, USA;

[3]Xinjiang Astronomical Observatory, Chinese Academy of Sciences, Ürümqi 830011, China;

[4]Beijing Institute of Control Engineering, Beijing 100190, China

Key Points:

- The centroids of the Ca and Fe line features during a flare in the soft X-ray (SXR) spectra observed by the Macau Science Satellite-1 exhibit blue shifts.
- Temperature and the blue-shifted velocity during the flare are derived by comparing the centroids with the synthesized line features from the latest CHIANTI atomic database.
- The peak velocity significantly exceeds the values previously reported, implying the entire shift of the SXR lines.

Citation: Li, J. P., Yang, X., Li, D., Shen, J. H., Yang, L., Wang, Y., Li, L. S., Shi, Y. Q., and Ji, H. S. (2025). Diagnostics of temperature and blue-shifted velocity using soft X-ray spectra from the Macau Science Satellite-1. *Earth Planet. Phys.*, *9*(3), 740–751. http://doi.org/10.26464/epp2025036

Abstract: Using the new soft X-ray data from the Macau Science Satellite-1, we studied a solar flare that occurred on 22 June 2023. We found that the centroids of the Ca (around 3.9 keV) and Fe (around 6.7 keV) line features exhibit a rapid shift toward higher energy channels during the flare's rising phase, followed by a gradual decrease during the decay phase. Through precise energy calibration, the centroids are determined with high accuracy. Temperature and velocity are then self-consistently derived by comparing the centroids with those calculated from the synthesized line features using the latest CHIANTI atomic database (ver. 10.1). The calculated maximum velocity reaches up to 710 ± 60 km s^{-1}, which significantly exceeds the previously reported values. Our results suggest that the entire shift of soft X-ray lines may occur during the process of chromospheric evaporation.

Keywords: Macau Science Satellite-1; solar flares, soft X-ray lines; chromospheric evaporation

1. Introduction

In the impulsive phase of solar flares, vast amounts of energy are transferred to the chromosphere through accelerated non-thermal electrons or thermal conduction fronts. In response, the chromospheric plasma is rapidly heated to temperatures higher than 10 MK and subsequently evaporates upward to fill the flare loop and emits in soft X-rays (SXRs). This process, known as chromospheric evaporation, plays a key role in the dynamics of flare energy release (Fisher, 1987).

Despite the high temperature of the heated plasma, the most distinctive feature of chromospheric evaporation is the upward flow of plasma from chromosphere into corona. Plenty works have been done using the high spectral resolution of SXR emission lines to derive the chromospheric evaporation velocity in the Solar Maximum Mission (SMM) and Yohkoh era. The X-ray resonance line of Ca XIX and Fe XXV usually show a blue-shifted component in the rising phase of disk flares, in addition to a nearly stationary core (Antonucci et al., 1982; Fludra et al., 1989; Doschek et al., 1996; Gan WQ and Watanabe, 1997). The velocity derived from the blue-shifted component relative to the stationary one reaches up to ~400 km s^{-1}. The blueshift is also observed in EUV spectral lines, which are formed at lower temperatures and exhibit lower velocities (Li Y and Ding MD, 2011; Young et al., 2013; Sellers et al., 2022). Some EUV spectral lines were found to be entirely blue shifted in a specific episode (Tian H and Chen NH, 2018). It seems that the velocity has a scaling relationship with temperature (Milligan and Dennis, 2009; Li D et al., 2022).

In simulations, chromospheric evaporation is investigated by modelling the hydrodynamic response of the solar atmosphere to a source of energetic electrons or thermal conduction (Somov et al., 1981; Longcope, 2014). In these models, the velocity significantly exceeds those derived from the observed line profiles. Fisher et al. (1984) showed that the upper limit to the chromospheric velocities is approximately 2.35 times coronal sound

First author: J. P. Li, jpli@pmo.ac.cn
Correspondence to: H. S. Ji, jihs@pmo.ac.cn
Received 30 DEC 2024; Accepted 13 MAR 2025.
First Published online 11 APR 2025.

speed. The maximum observed velocities for most flares seemed to be <25% of this limiting velocity. A crystal spectrometer achieves high wavelength resolution; however, absolute wavelength calibration is lost because the position of the rest wavelength on the detector depends on the angle between the emitting source and the instrument's optical axis (Bornmann, 1999). Therefore, it remains uncertain whether the "stationary component" observed previously truly stays stationary. Consequently, the maximum chromospheric evaporation velocities are also unresolved, which is crucial for understanding the heating mechanisms of solar flares.

With the launch of Macau Science Satellite-1 (MSS-1) (Zhang K, 2023), new SXR data are being recorded by silicon drift detectors (SDDs) with high energy resolution and efficiency, providing new insights into the dynamic process of chromospheric evaporation. This paper presents an analysis of the solar flare that occurred on June 22, 2023, using the SXR spectrum. We propose a method to derive the temperature and velocity from the centroids (E_c) of the Ca and Fe line features.

2. Observations and Data Reduction

The MSS-1 was successfully launched on May 21, 2023. It includes two subsatellites, MSS-1A and MSS-1B. The main objective of MSS-1A is to accurately measure the Earth's vector magnetic field, while MSS-1B is designed to monitor the solar activities and their impact on the Earth's space plasma. On 22 June 2023, MSS-1B successfully observed a solar flare in the National Oceanic and Atmospheric Administration (NOAA) active region (AR) 13341. It is an M4.9-class flare, starting at 23:29 UT and peaking at 23:44 UT, according to Geostationary Operational Environmental Satellites (GOES) soft X-ray flux. Figure 1a shows a full-disk Atmospheric Imaging Assembly (AIA) 171 Å image from the Solar Dynamics Observatory (SDO) mission taken at the peak time of the flare. The flare is located at the southeast region, highlighted by a red box. Figure 1b provides a close-up view of the boxed region, which shows brightening features of the flare, such as a solar jet, saturated flare loops and ribbons. In this study, we will focus on the disk-integrated SXR spectroscopy analysis of the flare. Therefore, the morphology evolution of the flare will not be emphasized.

The SXR detection unit (SXDU) onboard the MSS-1B was designed to measure the SXR spectrum of the Sun in the energy range of 1–20 keV (Shi YQ et al., 2023). Two X-ray SDDs with different effective areas are used in the SXDU to expand the observation ability for solar flares of different intensities. Each detector uses 2048 evenly spaced energy channels to record SXR spectrum data. Calibration with characteristic X-rays on the ground reveals a strong linear relationship between energy and channel (Zuo FC et al., 2024). The time cadence is as high as ~1 s and the energy resolution is approximately 150 eV at 5.9 keV. The MSS-1 circles the Earth in an near-circular orbit of 450 km altitude with a period of 96 min, in which about 36 min is occulted by the Earth. Thus, the observing time of the Sun is about 60 min in every period.

Figure 2 shows an overview of the SXR observations for this event. Several spectral lines are distinctly visible as apparently thick straight lines in the SXR spectrogram (see panel (a)). The recorded counts increase and extend to higher energy channels as the flare progresses. In panel (b), the total counts from all 2048 channels are integrated to show the time evolution of the SXR flux, which is consistent with the GOES SXR 0.5–4 Å flux. Based on the peak time of the GOES time derivative flux, we divided the flare process into two phases: the rising phase, occurring before the peak, and the decay phase, occurring after the peak. Panel (c) presents the integrated SXR spectrum over the full flare duration, revealing individual spectral lines. The most prominent lines, indicated by arrows, are from highly ionized Ca and Fe elements. We refer to them as the Ca and Fe line features, following Phillips (2004), as each is blended with a group of closely spaced lines. The L X-ray emission lines from ^{241}Am appear at higher channels (>1000, see Figure 2).

To analyze the Ca and Fe features in this event, we integrated the SXR spectra at 60-second intervals, balancing adequate line intensities with relatively high time resolution. Figure 3 and Figure 4 show the background-subtracted profiles of the Ca and Fe line features extracted from SXR spectra during the flare. A Gaussian

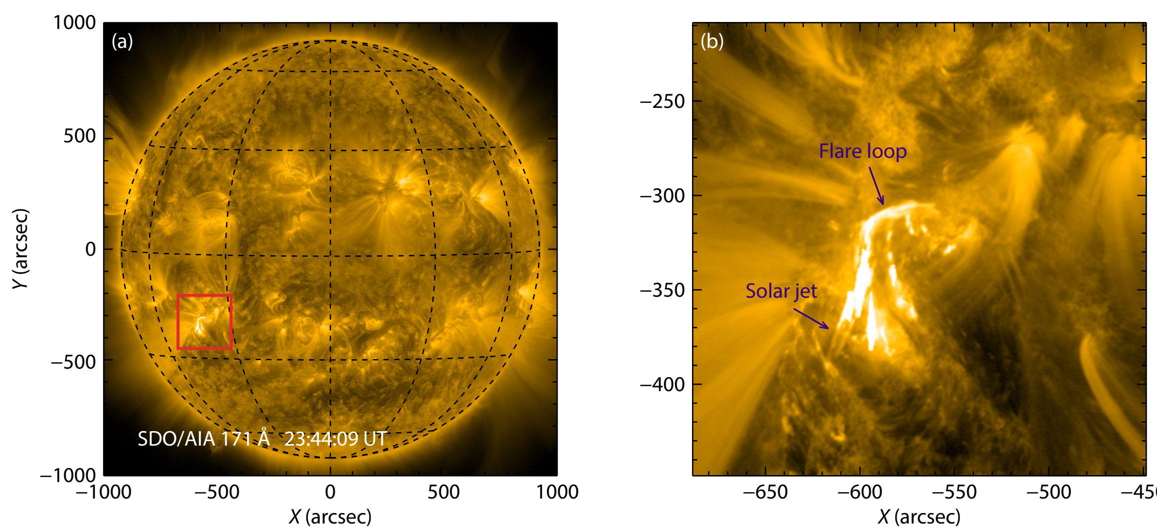

Figure 1. (a) Full-disk SDO/AIA 171 Å image, showing the location of the studied flare. (b) Close-up view of the flare highlighted by the red box in panel (a), showing detailed features of the event.

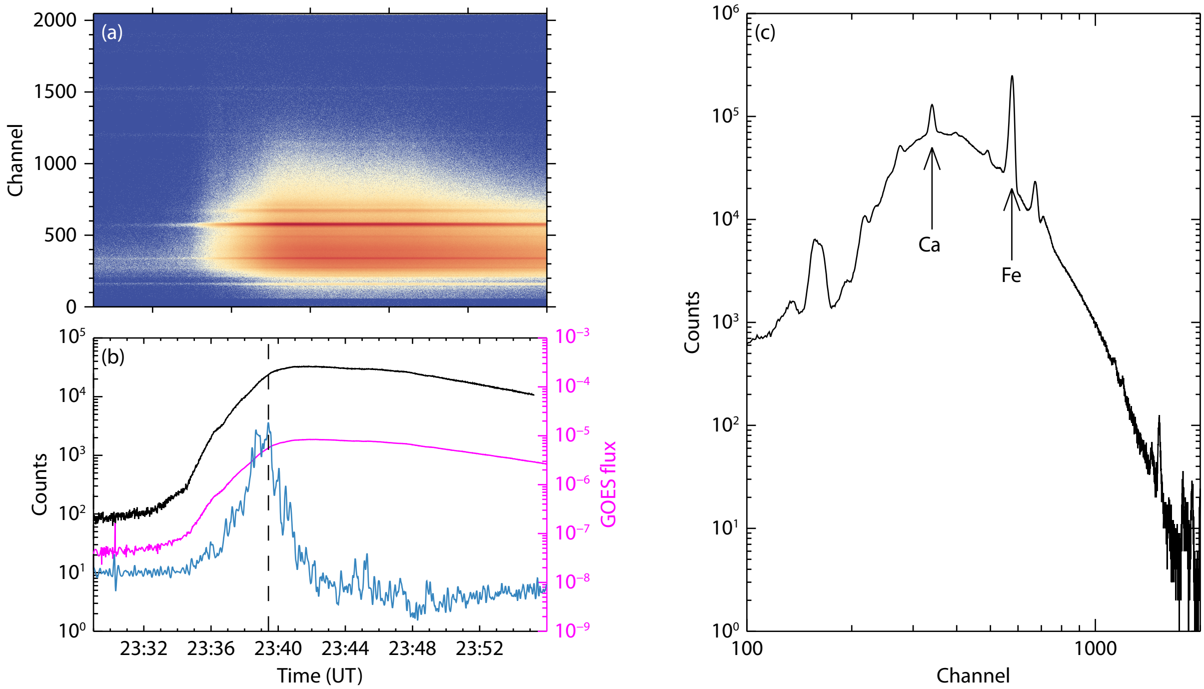

Figure 2. MSS-1B observations of the 2023 Jun 22 flare: (a) Spectral image of the flare at 0–20 keV. (b) Temporal evolution of the integrated SXR count flux across all channels (black), compared with the GOES SXR 0.5–4 Å flux (magenta). The time derivative of the GOES flux is shown in blue, with the peak time indicated in dashed lines. (c) Integrated spectra of the flare showing the Ca and Fe line features.

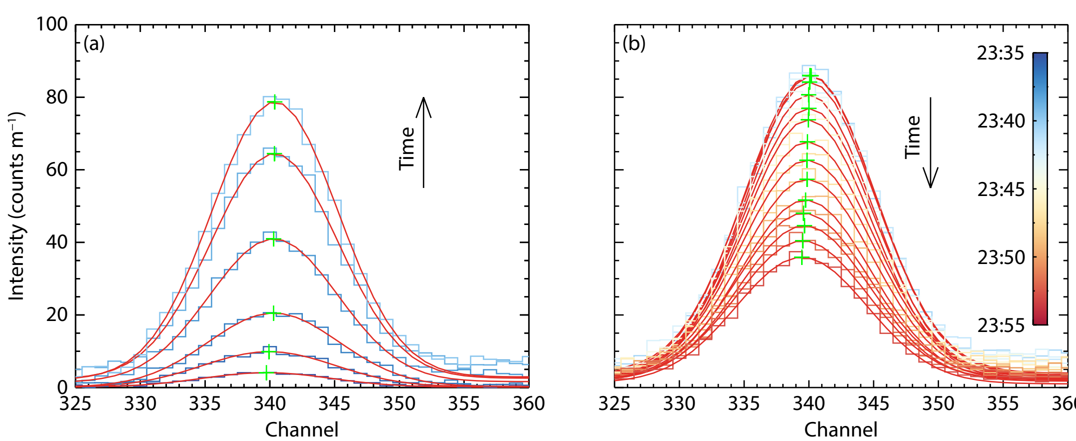

Figure 3. Line profiles of the Ca feature during the rising phase (pannel (a)) and the decay phase (pannel (b)), with centroids shifting with time. The observed profiles at different times (indicated by the colorbar) are displayed as histograms, with Gaussian fit lines overlaid in red. The fitted centroids are marked by green plus signs.

function is used for fitting each line feature to determine their centroids, which show a clear shift toward higher energies with time, indicating a progressive blue shift. This shift increases rapidly during the flare's rising phase and decreases gradually during the decay phase, compared to their initial positions.

The time profiles of the line centroids with 1σ uncertainties for the Ca and Fe features are shown in Figure 5. The blue shifts of two spectral lines follow a similar evolutionary pattern, i.e., rapid increasing during the rising phase followed by a gradual decrease in the decay phase. The maximum blue shift of the Ca line feature is approximately 2.2 channels, while the Fe line feature exhibits a much larger blue shift, exceeding 6 channels. Uncertainties in the fitted line centroids are closely related to their intensities. At the early stage of the flare, when the intensities are very weak, uncertainties are significantly larger. However, as the line intensities increase, uncertainties decrease to just a few percent of a channel.

3. Method and Results

Both the Ca and Fe line features consist of multiple distinct emission lines from highly ionized Ca and Fe atoms, each contributing to the total emission with its own temperature dependent intensity. As a result, the centroids of these features are highly sensitive to plasma temperature. Additionally, each emission line produced by moving plasma will be shifted to higher (if moving towards the observer) or lower (if moving away from the observer) energies

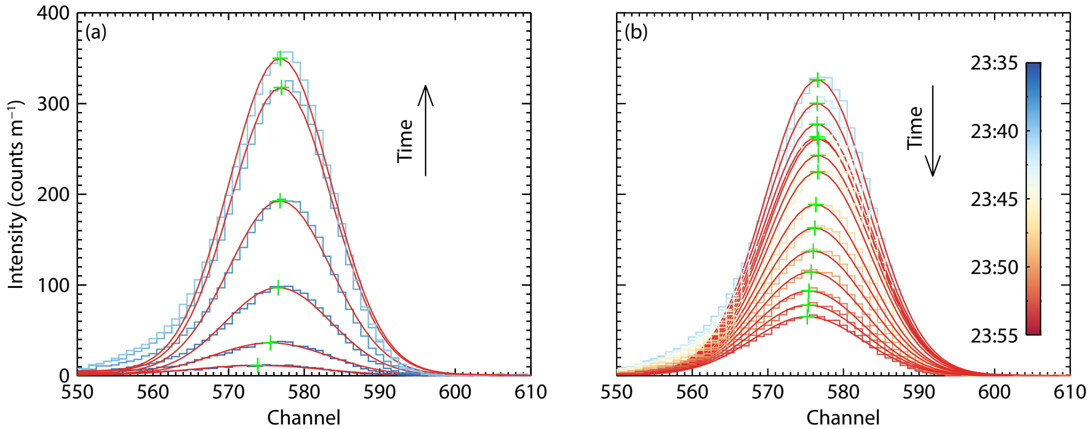

Figure 4. Same with Figure 3, but for the Fe line feature.

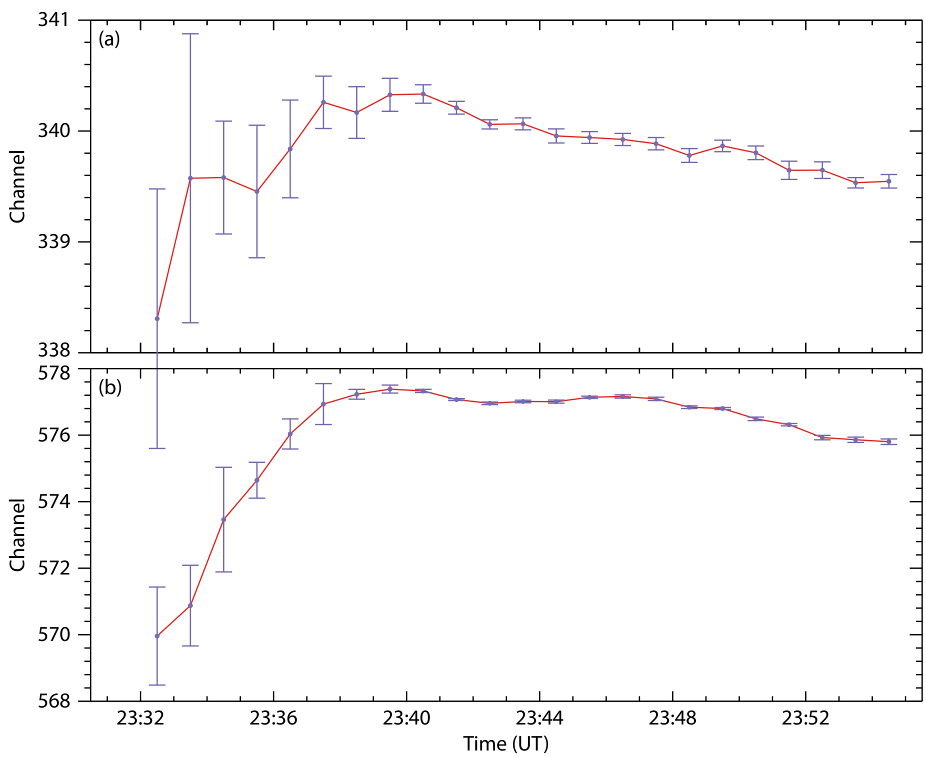

Figure 5. Temporal evolution of the centroids of the Ca (a) and Fe (b) line features, plotted with 1σ fitting uncertainties.

due to the Doppler effect. Thus, plasma motion is another key factor influencing the centroids of the Ca and Fe line features. These two factors, temperature and motion, are intricately linked. Accurate temperature diagnostics based on line feature shifts must incorporate the effects of plasma motion, and vice versa.

3.1 Temperature and Velocity Diagnostics

To investigate the influence of plasma temperature on the centroids of the line features, we utilized the latest version of Chianti code to synthesize the SXR spectra in the energy range of 3–10 keV for $6.5 < \log T < 7.5$, where both line features are well covered (see Appendix A). The Ca and Fe line features were extracted from the spectra, and centroids E_c were determined by fitting the line profiles with Gaussian functions. The values of E_c for the Ca and Fe line features are plotted against T in panel (a) and panel (b) of Figure 6, respectively. Both line features are very weak when $T \lesssim 10$ MK, though the profiles can still be fitted with Gaussian function. At higher temperatures, the values of E_c for both line features increase gradually with T, but at different rates. The total change of E_c for the Ca line feature is only about 0.01 keV over the range T = 10–30 MK, much smaller than the 0.1 keV change observed for the Fe line feather. As a result, the energy separation between the two line features also depends on T (see panel (c) of Figure 6) and closely resembles the behaviour of the Fe line feature.

To accurately extract physical quantities from the shifts, precise calibration is necessary to convert the channels into their corresponding energies. The ground calibration, performed using characteristic X-rays selected to evenly cover the energy range, shows a strong linear correlation. In orbit, calibration was carried out

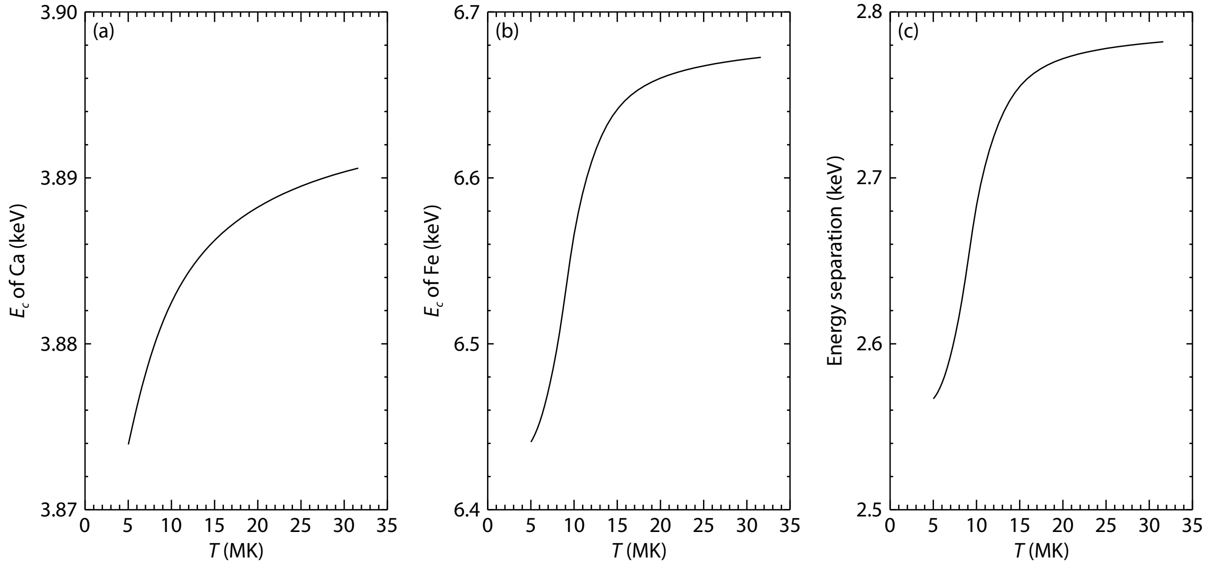

Figure 6. Centroid energies as a function of T for the Ca (a) and Fe (b) line features calculated using synthesized spectra from Chianti. Panel (c) shows the energy separation of the two line feature against T.

using spectral lines within the 1000 to 1980 channel range, derived from the sole ^{241}Am source carried with the MSS-1B satellite (see Appendix B). The calibration parameters, k and b, were derived by linearly fitting the centroids of ^{241}Am lines. This linear trend is expected to be extended to lower channels, especially for the Ca and Fe line features in channels 300–600. It is shown that the uncertainty associated with the value of k is 0.43%, reflecting a very high precision in the measurement. However, the value of b has an uncertainty of 5.89 channels, which will introduce a significant error in determining the line centroids. Thus, Calibration using ^{241}Am source itself is not enough, we need other restrictions.

Nevertheless, the energy separation between the Ca and Fe line features can be accurately determined, as it solely depends on k. If we assume that there is no plasma motion at a certain time, which is reasonable when chromospheric evaporation ceases in the flare's later phase, then E_c is entirely governed by T. At this time, the temperature T can be derived from the curve of energy separation against T (pannel (c) of Figure 6). Accordingly, E_c for the Ca and Fe line features can be subsequently derived from their respective relationships with T, as T is derived. At other times, E_c can be derived based on their shifts from that specific time. In such a way, E_c is determined at all times without relying on parameter b, whose uncertainty is considered unacceptable. The uncertainty of E_c at each time is given by the shift amount multiplied by the uncertainty of parameter k, which satisfies our requirements assuming we select an ideal time without any mass motion.

Using the above method, the E_c values for the Ca and Fe line features were determined at all times and are plotted as a function of time in Figure 7. Temperatures T were then derived by interpolating the values of E_c onto the T–E_c curves. Panel (a) of Figure 8

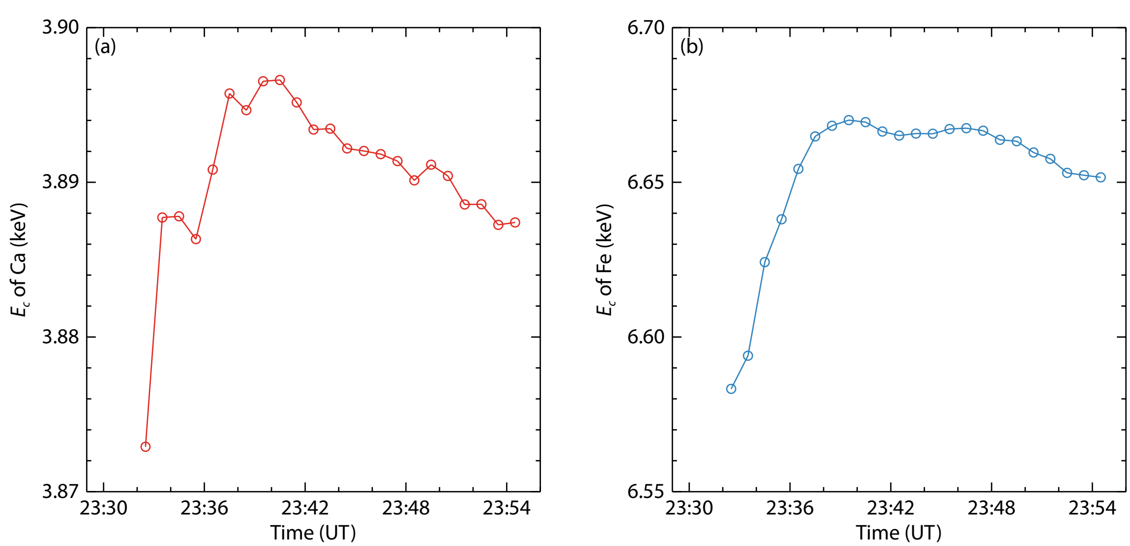

Figure 7. Time profiles of the calibrated centroid of the Ca (panel (a)) and Fe (pannel (b)) line features, showing the line shift with time.

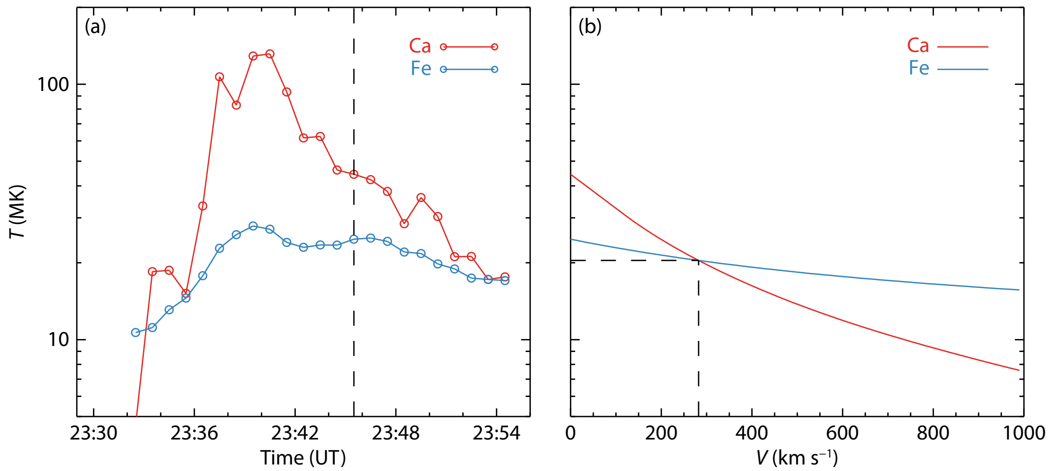

Figure 8. (a) Temporal evolution of temperatures derived individually from the centroids of the Ca (red) and Fe (blue) line features, revealing differences between them. (b) An example at 23:45 UT (dashed line in panel (a)) illustrating the temperature change with the introduced Doppler velocity for the Ca (red) and Fe (blue) line feature.

shows the time evolution of T inferred from the Ca and Fe line features, respectively. The plasma temperature from the two line feathers exhibits a similar pattern, i.e., a rapid increase during the impulsive phase followed by a gradual decline in the decay phase. However, the T values derived from different line features are generally not identical, with the values from the Ca line feature much higher than those from the Fe line feature. The temperature difference reaches highest around the peak of the flare, at which time the T value from the Ca line feature becomes extraordinary high, exceeding 100 MK. Such high-temperature plasma seems unlikely to be produced in the chromospheric evaporation process. These facts suggest that mass motions must play an important role in the shift of E_c, in addition to T.

Mass motions along the line of sight can induce a Doppler shift in E_c, reducing the contribution of T and consequently lowering its values. In panel (b) of Figure 8, we show an example at 23:45:30 UT (marked in dashed lines of panel (a)) for the changes of T as a function of the introduced line-of-sight velocity (red curve is for the Ca line feature, blue curve is for the Fe line feature). It is evident that T decreases as increasing velocity (positive value indicating upward motion) for both line features, with the decline rate being steeper for the Ca than the Fe line feature. As a result, the two curves of T against v intersect at the point (T = 20.4 MK, v = 282 km s^{-1}). This means that a blue-shifted velocity of 282 km s^{-1} can bring the electron temperatures T from the two line features into agreement. In this way, the chromospheric evaporation velocities can be inferred at all times.

Finally, we self-consistently derived the temperature T and the line-of-sight velocity v by combining the shifts in E_c of the Ca and Fe line features. Figure 9 shows the time profiles of T and v for this event. In the impulsive phase, the temperature increases in a pattern similar to that derived from GOES (magenta in panel (a)), though it is slightly faster. At the peak time, the temperature is approximately 1.5 MK higher than that from GOES. However, during the decay phase, a prominent bulge appears as the temperature decreases, with the values even exceeding that at the peak time. Upon closer inspection, the GOES temperature curve also shows a bulge, though it is much weaker. We are not sure whether the temperature during the decay phase can truly exceed that at the peak time, due to the relatively larger uncertainty in temperature measurement, which will be addressed later. In panel (b), we can see that the line-of-sight velocity rises rapidly during the impulsive phase, then drops quickly in the decay phase, while the temperature still remains high. This behavior is consistent with the chromospheric evaporation scenario, in which the evaporation process slows down as the evaporated material fills the flare loop, yet the temperature remains high. Several velocity spikes appear during the decline, which may correspond to small-scale events, such as jets. To our surprise, the peak value of the velocity reaches 710 km s^{-1}, significantly higher than the values reported previously.

3.2 Uncertainty Estimation

Uncertainties in temperature and line-of-sight velocity are mainly caused by calibration errors and fitting uncertainties. To demonstrate their impacts, we examine the observation at velocity peak time, showing how these uncertainty sources affect the derived temperature and velocity. In energy calibration, the 1σ uncertainty of parameter k was found to be approximately 0.4%. Thus, in panel (a) of Figure 10, we plotted the derived temperature (blue curve) and velocity (red curve) as a function of the k error within the range of ±0.4%. It is seen that the temperature increases with k, while the velocity decreases. This fact can be understood that the increase of k amplifies the energy separation between the Ca and Fe line features, leading to a higher temperature at the reference time. Temperature varies from 15 to 24.4 MK with a median value being 17.6 MK (k_{error} = 0). Consequently, the maximum temperature uncertainty is 6.7 MK, which is a very high value. But for the velocity, it varies from 701 to 712 km s^{-1}, with the median value being 710 km s^{-1}. The maximum velocity uncertainty is 9 km s^{-1}, only about 1.3% of the median value.

When considering the uncertainties of E_c due to Gaussian fitting, the derived temperature from E_c also carries associated uncertainties. As a result, the T–V curves for the Ca and Fe line features in panel (b) of Figure 8 will be replaced by two thicker curves associ-

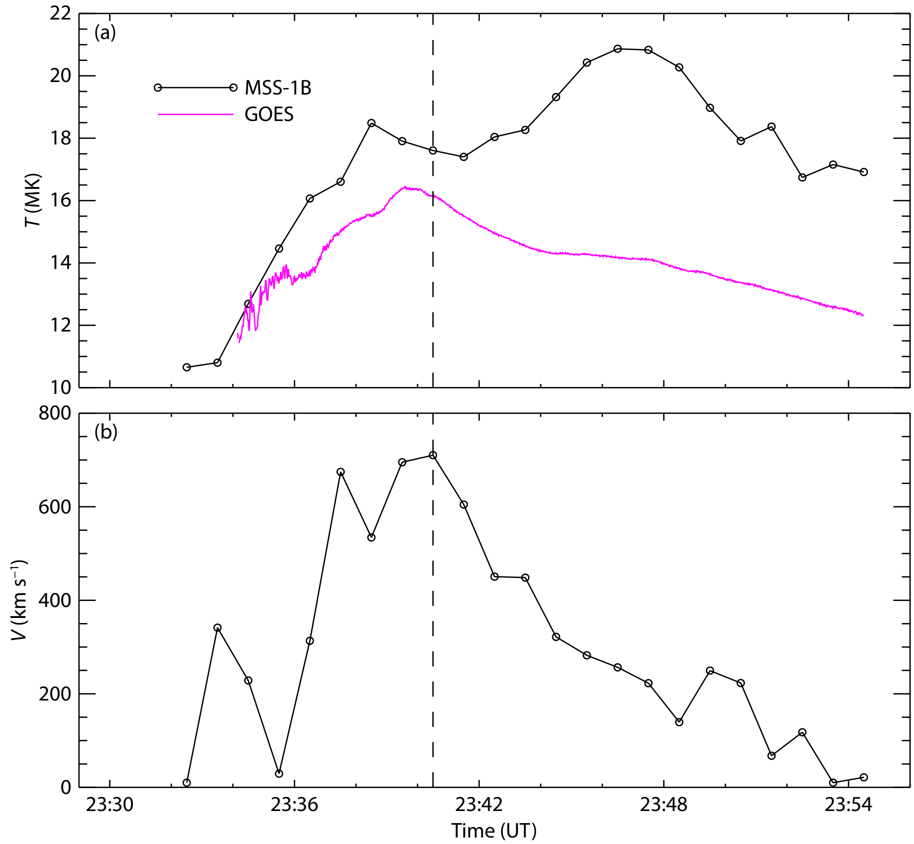

Figure 9. (a) Temporal evolution of the temperature derived from the E_c values of the Ca and Fe line features, with Doppler effect removed. For comparison, the temperature derived from the GOES SXR flux is also shown, represented in pink. (b) Temporal evolution of the extracted line-of-sight velocity. Dashed lines indicate the peak velocity time.

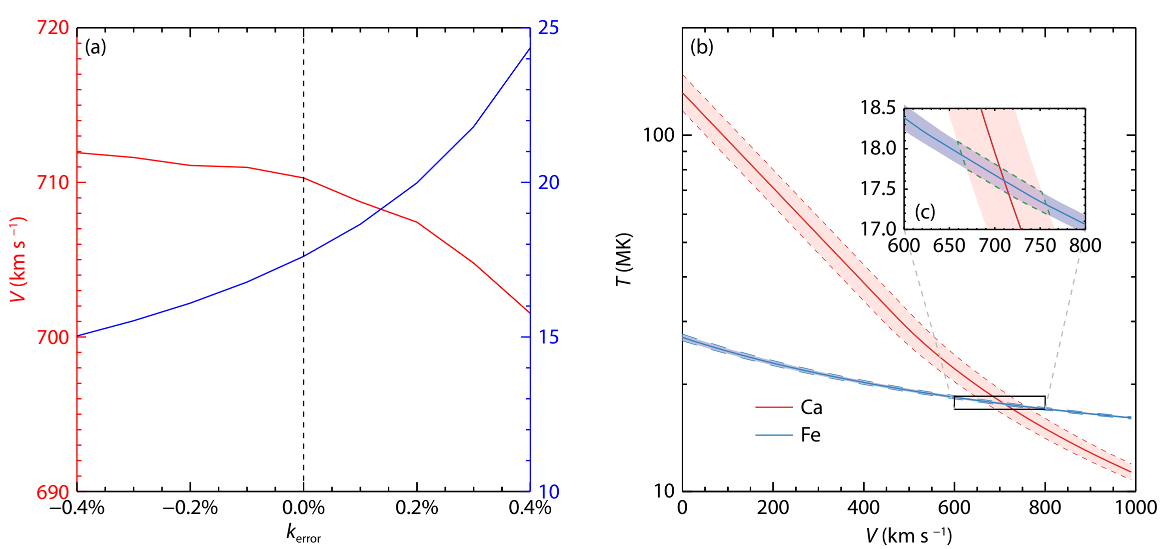

Figure 10. (a) Variation of the derived velocity (red) and temperature (blue) as a function of the calibration parameter k error over the 1σ range at velocity peak time. (b) Variation of temperatures derived from the Ca line feature (red) with uncertainties (filled region in rose) and the Fe line feature (blue) with uncertainties (filled region in purple) as a function of velocity. The intersection region is outlined with a grey box. (c) Close-up view of the intersection region, showing the range of temperature and velocity.

ated with the temperature uncertainty, as shown in panel (b) of Figure 10. Consequently, the intersection of the two curves is replaced by a region (in the black box), rather than a single point. Panel (c) presents a detailed, extended view of the intersection region, where the temperature ranges from 17.3 to 18.1 MK, and the velocity spans from 659 to 761 km s^{-1}. Thus, the temperature and velocity uncertainty are estimated to be 0.5 MK and 51 km s^{-1}, respectively.

The temperature seems more sensitive to the calibration parameter k, while the velocity is more strongly influenced by E_c. Combined with the two sources of uncertainty, we derived the temperature at velocity peak time to be 17.6 MK with an uncertainty of 7.1 MK, the velocity to be 710 km s^{-1}, with an uncertainty of 60 km s^{-1}. The total uncertainties are obtained by adding the individual contributions for simplicity.

4. Summary and Conclusion

We have analyzed the SXR spectra of the 2023 Jun 22 flare using new data from the MSS-1B satellite. Precise energy calibration of the SXR data are achieved by utilizing a set of selected lines from the radiative source ^{241}Am carried onboard the satellite, combined with the assumption that chromospheric evaporation ceases at a specific time. From the SXR spectra, the Ca and Fe line features are extracted. By applying Gaussian fitting, we derived the centroids E_c for both line features. The time profiles of E_c show an increasing during the rising phase of the flare, followed by a decrease in the decay phase. Using the latest version of Chianti atomic database, we synthesize the profiles of Ca and Fe line features at different temperatures under the isothermal assumption, establishing a relationship between E_c and T. To ensure the temperatures derived from individual line features equal with each other, the inclusion of velocity is necessary to account for part of the shifts in E_c. Finally, we derive the self-consistent temperature and velocity for this event.

Each of the Ca and Fe line features consists of a group of closely spaced lines that would appear as a single blended profile when observed with a spectrometer of insufficient resolution. The rise of E_c in these profiles during flares is barely measured by broadband spectrometer before the launch of MSS-1B. Although the energy resolution of RHESSI is adequate to detect such a rise, an unexpected gain variation with the count rate in the RHESSI detectors prevents this measurement (Phillips, 2004). Thanks to the high energy resolution of SDDs onboard MSS-1B, which is approximately 8 times higher than that of RHESSI, but not enough to distinguish individual lines. Such particular resolution, combined with high efficiency, enables MSS-1B to successfully detect these shifts during flares.

According to the shifts of these two line features, we self-consistently derived the temperature and velocity of evaporated plasma. The most surprising finding is that the peak velocity reaches up to 710 ± 60 km s^{-1}. This value significantly exceeds 400 km s^{-1}, the value obtained from crystal spectrometers onboard SMM and Yohkoh (e.g., Antonucci et al., 1984; Kato et al., 1998). In these observations, the resonance lines of Ca XIX and Fe XXV usually show a weaker blue-shifted component that disappears after the rising phase (Doschek, 1990). Due to the generally poor absolute wavelength calibration of these instruments, velocity is determined from the shift of the blue-shifted component relative to the stationary one, rather than from the absolute shift of the line position. Our results suggest that the “stationary” component may not be truly static, but could exhibit great entire shift.

Despite the multi-thermal nature of the solar atmosphere, an isothermal approximation is applied in the SXR spectra synthesis. The lines that contribute to the Ca and Fe features are optically thin and highly sensitive to temperature. As a result, emissions from higher temperatures dominate the overall intensity contribution, while from lower temperatures contributes little. We consider this is a reasonable approximation, as it effectively reflects the temperature and velocity of the hottest evaporated plasma. Allowing for multi-thermal plasma would increase the velocity error. However, we believe this error is likely limited, as the temperature uncertainty is already quite large. The maximum plasma velocity even with projection effect reaches 700 km^{-1}. This unusually high speed suggests that the chromospheric evaporation process could be more explosive than previously expected, with a larger fraction of the energy being converted into kinetic energy. The high-resolution soft X-ray data, with better cadence and more precise spectral resolution recorded by MSS-1B, demonstrates significant potential for advancing the study of solar activity and offering new insights into the dramatic energy processes of solar flares.

Acknowledgments

This work was funded by NSFC under grants 12250014, 12273101. This work was also supported by the Macao Foundation. H. Ji thanks Xinjiang Uygur Autonomous Region for the support through “Tianchi Talent” special expert project. J. Shen was also supported by Natural Science Foundation of Xinjiang Uygur Autonomous Region under grant 2024D01E38. CHIANTI is a collaborative project involving George Mason University, the University of Michigan (USA), University of Cambridge (UK) and NASA Goddard Space Flight Center (USA). We gratefully acknowledge the Laboratoire National Henri Becquerel for providing the usage of COLEGRAM software. We are grateful to the anonymous referees for their constructive input.

Supplementary Materials

Appendix A. Spectral Synthetic

The line feature around ~6.7 keV is made up of many individual emission lines from highly ionized Fe atoms (Fe XIX to Fe XXV) at electron temperatures T greater than 10 MK (Phillips, 2004). Each of the lines has its own temperature dependence of the contribution to the total emission of the Fe line feature. The energies of these lines are so closely spaced that broadband spectrometer observations, such as those from RHESSI or MSS-1B, cannot resolve them individually and instead detect them as a single blended broad line. As the electron temperature increases, emission lines from higher ionization states become more prominent, leading to the intensity contributions from higher-energy lines dominate. As a result, the centroid of ~6.7 keV line feature shows an apparently shift to higher energies, i.e., blue shift, with the increase of temperature (Li D et al., 2024). Using Chianti atomic database and code (ver. 4.2), Phillips (2004) synthesized the spectra in the 3.8–10 keV range at different temperatures and derived the relationship between centroids and temperatures. The validity is checked by high-resolution observations made with the SMM Bent Crystal Spectrometer and the Yohkoh Bragg Crystal Spectrometer. The line feature around ~3.9 keV is also made up of many individual emission lines from highly ionized Ca atoms (Ca

XVIII to Ca XX), similar to the Fe line feature. Therefore, the centroids of both Ca and Fe line features are highly dependent on plasma temperature.

Followed by the method of Phillips (2004), we use the latest version of Chianti atomic database (ver. 10.1) (Zanna et al., 2021), to sythesize the spectra in energy range of 3–10 keV for $6.5 < \log T < 7.5$, where the two line features are well covered. An isothermal approximation is assumed, which means that all plasma is at a single temperature T. Under such an assumption, the intensity $I(\lambda)$, of an optically thin spectral line is:

$$I(\lambda) = C(T, \lambda, N_e) Ab(X) EM, \tag{A1}$$

where, $C(T, \lambda, N_e)$ is the contribution function, containing the relevant atomic parameters, N_e is the electron density, $Ab(X)$ is the elemental abundance of X relative to Hydrogen, EM is the column emission measure. It is found that the line shape is mainly determined by the contribution function, while $Ab(X)$ and EM only affect the line intensity. Additionally, Ca and Fe lines are not sensitive to electron density. Thus, we arbitrarily set the emission measure EM to 10^{30} cm^{-5} and electron density N_e to 10^9 cm^{-3}. The spectra were synthesized for only Ca and Fe ions without continuum contributions. A bin size of 11.7 eV and an instrumental full width at half maxima (FWHM) of 150 eV were set to match the spectral resolution of MSS-1B.

Pannel (a) in Figure A1 shows an example of the synthesized intensity-normalized Ca line feature at $\log T = 7.0$ and $\log T = 7.4$, respectively. The five most intense lines contributing to the total profile at each temperature are indicated by vertical lines. As the temperature increases from $\log T = 7.0$ to $\log T = 7.4$, the relative intensities of these lines change, with higher-energy lines dominating, and some lines even dropping out of the top five intense lines. As a result, the centroid of the Ca profile shifts to higher energy. For the Fe line feature, the shift in the centroid is even more pronounced (see panel (b)), where the original five most intense lines are entirely replaced by other higher-energy lines. Therefore, the centroids of the Ca and Fe line features are highly dependent on temperature.

Appendix B. Calibration for the Energy

Precise calibration of energy (or wavelength) is crucial to derive reliable and meaningful physical quantities from solar spectra, especially in high-energy ranges or short wavelengths, such as those encountered in SXRs. Fortunately, the MSS-1 is equipped with a radioactive source of americium-241 (^{241}Am), which can be used for calibration purpose. The radionuclide ^{241}Am undergoes alpha decay to ^{237}Np with a half-life of 432.6 years, during which a series of L X-ray emission lines in the energy range of 10–20 keV are emitted steadily. Thus, the ^{241}Am source has ever been extensively used for the efficiency calibration of semiconductor X-ray detectors (Campbell and McNelles, 1974).

In this paper, we utilize ^{241}Am spectra to calibrate the energy response of the detector, i.e., establishing the relationship between channel numbers and their corresponding energy values. The entire day's observation of 2023 June 22 was selected to accumulate sufficient SXR photon counts. Panel (a) of Figure B1 shows the time evolution of total flux accumulated from all the 2048 energy channels. It is clearly shown that the flux undergoes a dramatic decrease, dropping to below 20 counts whenever the satellite enters the Earth's shadow. During these periods, most of the SXR counts from the Sun are blocked by Earth, while the left counts are purely emitted from the ^{241}Am source carried by MSS-1B. This occurs every 96 minutes, with the satellite spending around 36 minutes in the shadow in each orbit. Therefore, we use a 20-count threshold (blue dashed line in panel (a) of Figure B1) to identify the periods of the satellite being in the Earth's shadow and then integrate the spectra from these intervals. This approach ensures that we could obtain a pure ^{241}Am spectrum, free from the influence of the Sun's radiation. Panel (b) of Figure B1 shows the pure ^{241}Am spectrum integrated by 7 orbits' time intervals, in which multi-peaks between 1000–1980 channels (red dashed lines) are clearly displayed. Among these peaks, the two most intense ones are at 11.87 and 13.94 keV, respectively.

In order to derive the centroids of the multiple peaks, the ^{241}Am spectra were processed with the software Colegram (Ménesguen and Lépy, 2021) in a region of interest (ROI) between 1000 and 1980 channels. Colegram is a freely available spectrometry soft-

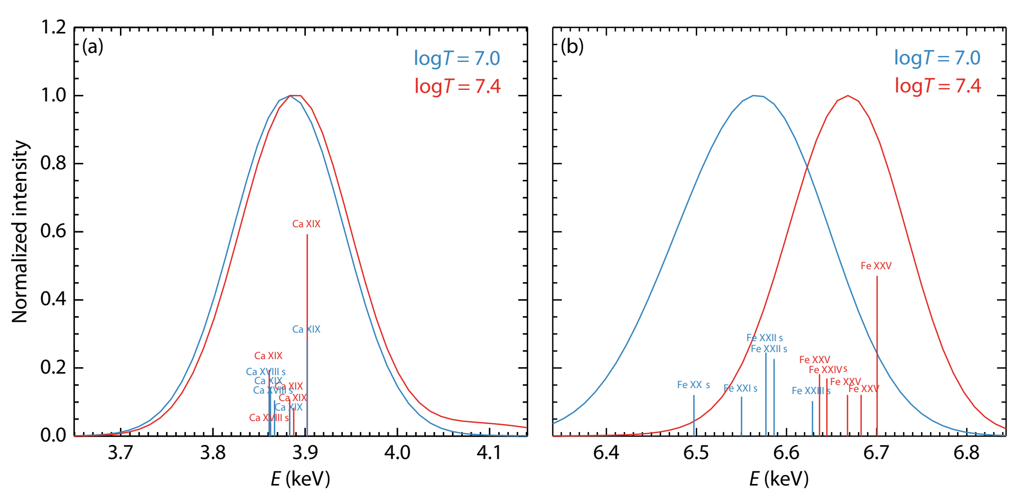

Figure A1. (a) Synthesized Ca line feature at $\log T = 7.0$ (blue) and $\log T = 7.4$ (red), with the five most intense lines (indicated by vertical lines) at each temperature. (b) Same as panel (a), but for the synthesized Fe line feature.

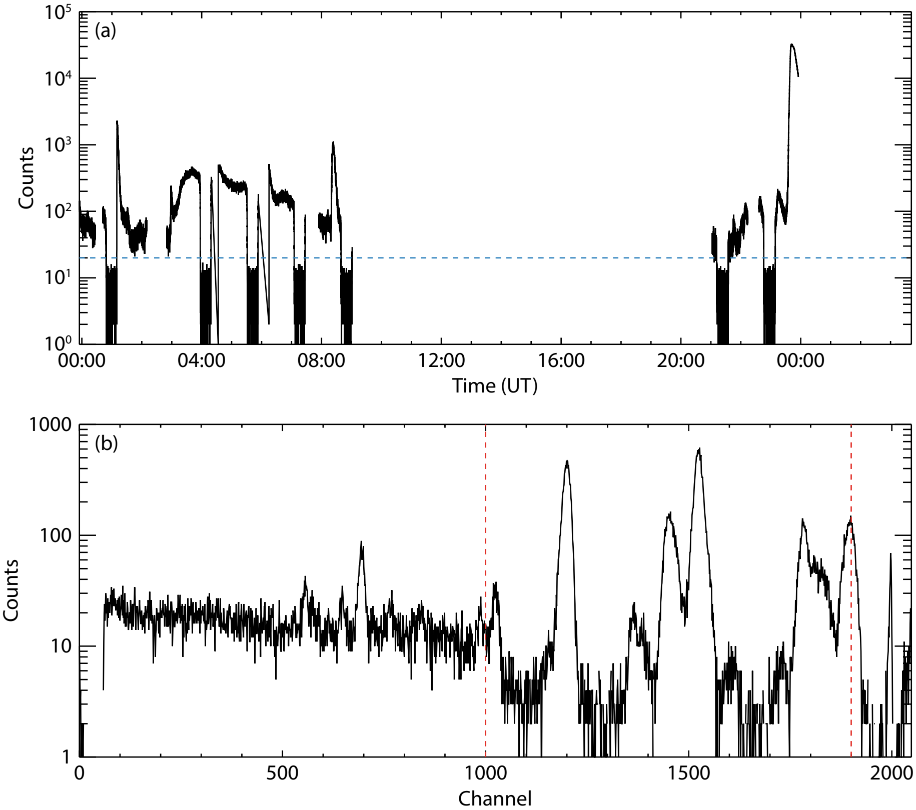

Figure B1. (a) SXR fluxes (integrated by all channels) for the whole day of 2023 Jun 22. The blue dashed line represents a 20-count threshold, below which the satellite is in the Earth's shadow. (b) SXR spectrum integrated by all the times with fluxes lower than 20 counts per second, as indicated by the blue dashed line in panel (a). Multi-peaks of ^{241}Am are clearly shown between red dashed lines.

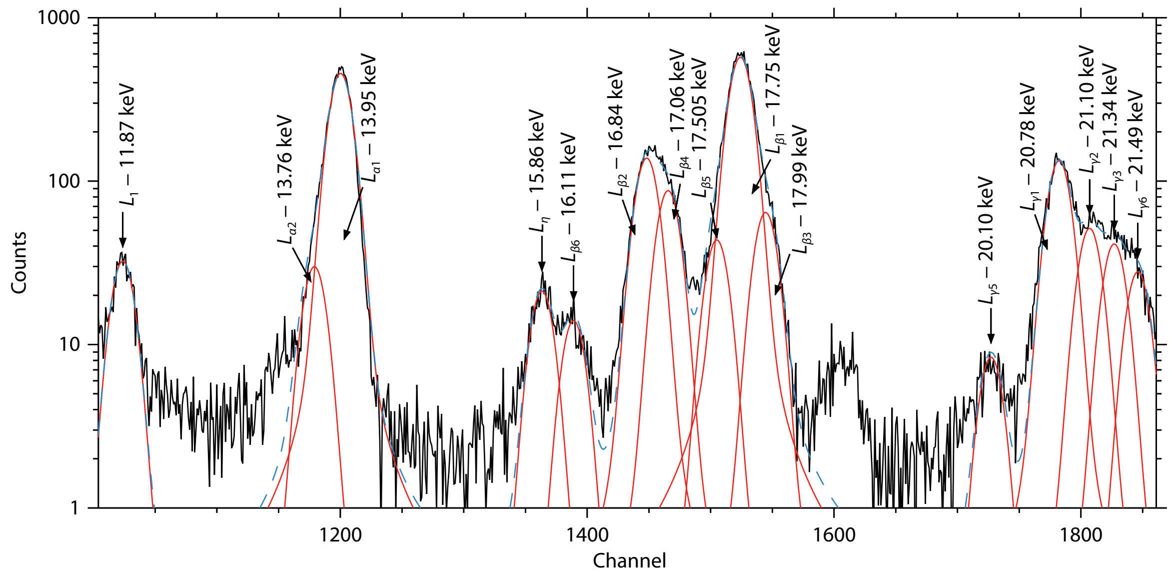

Figure B2. ^{241}Am profiles showing multi-peaks, fitted by Voigt functions (red lines) in 10–20 keV energy range.

ware with a user-friendly interface developed at the Laboratoire National Henri Becquerel. Users can manually insert peaks in the ROI window and choose from various fitting functions depending on the spectrum type, utilizing a non-linear least-squares fitting method. We use a Voigt function, which is the convolution of a Lorentzian and a Gaussian function, for fitting each peak. The Lorentzian component accounts for the natural line width due to the finite lifetime of the atom's excited state, while the Gaussian function reflects the contribution from the detector's energy resolution, which is much broader than the line natural width. The detector's energy resolution is influenced by several factors, including the Fano factor, readout electronic noise, and temperature fluctuations. The Lorentzian natural widths are fixed to 1 channel, approximately 12 eV, same as the value used by Lépy et

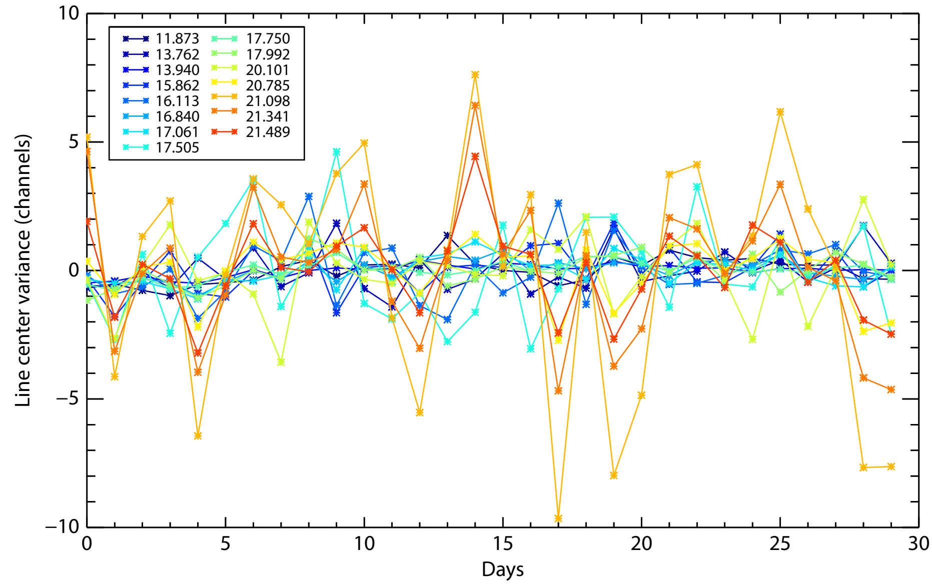

Figure B3. Variation in line center positions for different ^{241}Am lines over a 30-day period, with each line represented by a distinct color to highlight individual trends and fluctuations.

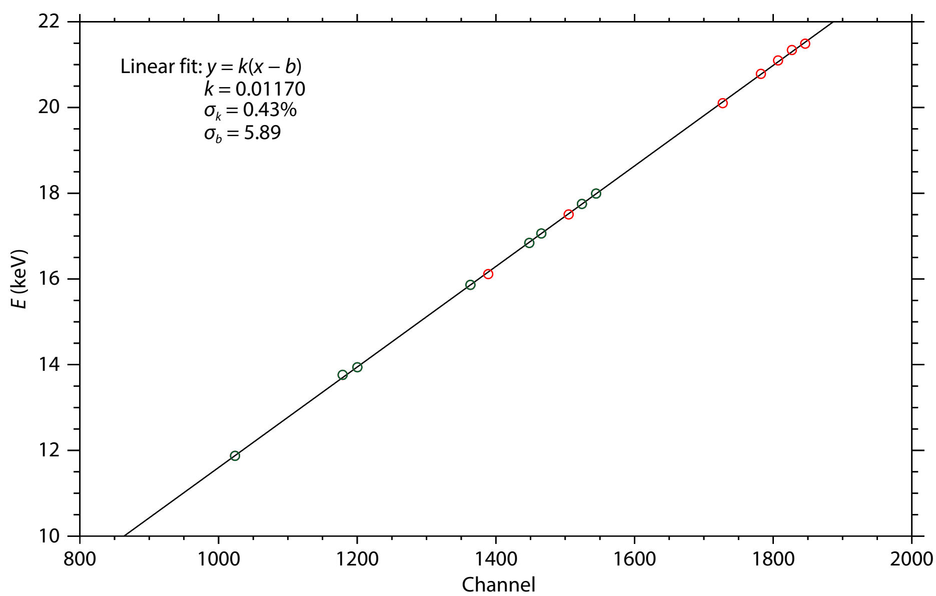

Figure B4. Linear fit of the peaks using 8 lines (dark green circles). The left 7 line peaks (red circles) are excluded from the fit due to their larger uncertainties. $y = k(x - b)$ is linear fit equation. k is slope. σ_k is relative uncertainty of slope k. σ_b is uncertainty of offset b.

al. (1994). Other parameters of the Voigt function are set to be free. Based on Figures 3 and 4 in Lépy et al. (2008) which illustrate the fitting of an ^{241}Am spectrum, we insert 15 peaks at corresponding positions. The fitting results are presented in Figure B2, with each peak marked. The exact energy values of the peaks are taken from Table 3 in Rodrigues et al. (2023). Note that the spectrum is not intensity-calibrated. However, it is expected to have a negligible impact on determining the centroids of the peaks, as each peak has a very narrow width. Uncertainties of the centroids are obtained simultaneously with the software. It is clear that the position uncertainties for lines with stronger intensity (e.g., peaks at 13.95 and 17.75 keV) or a distinguishable peak (e.g., peak at 11.87 keV) are smaller, while for those with weaker intensity or overlapped with others are larger.

To further assess the stability of the derived centroids for each line, we fit the ^{241}Am spectra over 30 consecutive days using the same method. Figure B3 displays the variance of each line (indicated by different color) across the 30-day period. It is worth noting that the daily variance for weak or overlapping peaks is significantly larger (around 5 channels), even when the uncertainties themselves are small. These fluctuations are likely caused by instrumental effects, particularly in cases where the observed photon counts are very low.

For accurate energy calibration, peaks as many as possible are desirable. However, those with large uncertainties and daily variances do not contribute to improving the accuracy. Therefore, peaks with a daily variance greater than 1 channel were excluded from the fitting process. Ultimately, 8 from the 15 identified peaks were selected for fitting.

Figure B4 illustrates a linear relationship between the positions in channel (*x-axis*) and the corresponding energies in keV (*y-axis*) for the 15 peaks. A linear fit is applied to the selected eight peaks. The linear function follows the equation:

$$y = k(x - b), \tag{B1}$$

where k denotes the slope of the straight line and b is the offset where it intersects the *x-axis* (the point where energy is 0 keV). The uncertainties associated with k and b are 0.43% and 5.89, respectively.

References

Antonucci, E., Gabriel, A. H., Acton, L. W., Culhane, J. L., Doyle, J. G., Leibacher, J. W., Machado, M. E., Orwig, L. E., and Rapley, C. G. (1982). Impulsive phase of flares in soft X-ray emission. *Sol. Phys.*, *78*(1), 107–123. https://doi.org/10.1007/BF00151147

Antonucci, E., Gabriel, A. H., and Dennis, B. R. (1984). The energetics of chromospheric evaporation in solar flares. *Astrophys. J.*, *287*, 917–925. https://doi.org/10.1086/162749

Bornmann, P. L. (1999). Chromospheric evaporation theory. In K. T. Strong, et al. (Eds.), *The Many Faces of the Sun*: *A Summary of the Results from NASA'S Solar Maximum Mission* (pp. 301). New York: Springer.

Campbell, J. L., and McNelles, L. A. (1974). Americium-241 as a low-energy photon intensity standard. *Nucl. Instrum. Methods*, *117*(2), 519–532. https://doi.org/10.1016/0029-554X(74)90301-2

Del Zanna, G., Dere, K. P., Young, P. R., and Landi, E. (2021). Chianti — An atomic database for emission lines. XVI. Version 10, further extensions. *Astrophys. J.*, *909*(1), 38. https://doi.org/10.3847/1538-4357/abd8ce

Doschek, G. A. (1990). Soft X-ray spectroscopy of solar flares: an overview. *Astrophys. J.*, *73*, 117. https://doi.org/10.1086/191443

Doschek, G. A., Mariska, J. T., and Sakao, T. (1996). Soft X-ray flare dynamics. *Astrophys. J.*, *459*(2), 823. https://doi.org/10.1086/176946

Fisher, G. H., Canfield, R. C., and McClymont, A. N. (1984). Chromospheric evaporation velocities in solar flares. *Astrophys. J.*, *281*, L79–L82. https://doi.org/10.1086/184290

Fisher, G. H. (1987). Explosive evaporation in solar flares. *Astrophys. J.*, *317*, 502–513. https://doi.org/10.1086/165294

Fludra, A., Lemen, J. R., Jakimiec, J., Bentley, R. D., and Sylwester, J. (1989). Turbulent and directed plasma motions in solar flares. *Astrophys. J.*, *344*, 991–1103. https://doi.org/10.1086/167866

Gan, W. Q., and Watanabe, T. (1997). Line shifts observed by BCS/Yohkoh. *Adv. Space Res.*, *20*(12), 2319–2322. https://doi.org/10.1016/S0273-1177(97)01052-1

Kato, T., Fujiwara, T., and Hanaoka, Y. (1998). X-Ray spectral analysis of *Yohkoh* bragg crystal spectrometer data on a 1992 September 6 flare: The blueshift component and ion abundances. *Astrophys. J.*, *492*(2), 822–832. https://doi.org/10.1086/305047

Lépy, M., Duchemin, B., and Morel, J. (1994). Comparison of experimental and theoretical LX — ray emission probabilities of ^{241}Am, ^{239}Pu and ^{240}Pu. *Res. Sect. A: Accel. Spectrom. Detect. Assoc. Equip.*, *353*(1-3), 10–15. https://doi.org/10.1016/0168-9002(94)91591-1

Lépy, M., Plagnard, J., and Ferreux, L. (2008). Measurement of ^{241}AM *LX*-ray emission probabilities. *Appl. Radiat. Isot.*, *66*(6-7), 715–721. https://doi.org/10.1016/j.apradiso.2008.02.078

Li, D., Hong, Z. X., and Ning, Z. J. (2022). Simultaneous observations of chromospheric evaporation and condensation during a C-class flare. *Astrophys. J.*, *926*(1), 23. https://doi.org/10.3847/1538-4357/ac426b

Li, D., Li, J. P., Shen, J. H., Song, Q. W., Ji, H. S., and Ning, Z. J. (2024). Long-period energy releases during a C2.8 flare. *Astron. Astrophys.*, *690*, A39. https://doi.org/10.1051/0004-6361/202450622

Li, Y., and Ding, M. D. (2011). Different patterns of chromospheric evaporation in a flaring region observed with *Hinode*/EIS. *Astrophys. J.*, *727*(2), 98. https://doi.org/10.1088/0004-637X/727/2/98

Longcope, D. W. (2014). A simple model of chromospheric evaporation and condensation driven conductively in a solar flare. *Astrophys. J.*, *795*(1), 10. https://doi.org/10.1088/0004-637X/795/1/10

Ménesguen, Y., and Lépy, M. C. (2021). COLEGRAM, a flexible user-friendly software for processing of ionizing radiation spectra. *Nucl. Instrum. Methods Phys. Res. Sect. A: Accel. Spectrom. Detect. Assoc. Equip.*, *1003*, 165341. https://doi.org/10.1016/j.nima.2021.165341

Milligan, R. O., and Dennis, B. R. (2009). Velocity characteristics of evaporated plasma using *Hinode*/EUV imaging spectrometer. *Astrophys. J.*, *699*(2), 968–975. https://doi.org/10.1088/0004-637X/699/2/968

Phillips, K. J. H. (2004). The solar flare 3.8-10 keV X-ray spectrum. *Astrophys. J.*, *605*(2), 921. https://doi.org/10.1086/382523

Rodrigues, M., Loidl, M., and Pierre, S. (2023). Determination of absolute Np L x-ray emission intensities from ^{241}Am decay using a metallic magnetic calorimeter. *Metrologia*, *60*(2), 025005. https://doi.org/10.1088/1681-7575/acb99f

Sellers, S. G., Milligan, R. O., and James McAteer, R. T. (2022). Call and response: a time-resolved study of chromospheric evaporation in a large solar flare. *Astrophys. J.*, *936*(1), 85. https://doi.org/10.3847/1538-4357/ac87a9

Shi, Y. Q., Li, L. S., Chen, J. W., Zuo, F. C., Zhang, X. P., Mei, Z. W., and Zhang, K. (2023). Design of the solar X-ray detector for the Macau Science Satellite-1B. *Earth Planet. Phys.*, *7*(1), 125–130. https://doi.org/10.26464/epp2023018

Somov, B. V., Syrovatskii, S. I., and Spektor, A. R. (1981). Hydrodynamic response of the solar chromosphere to an elementary flare burst I: Heating by accelerated electrons. *Sol. Phys.*, *73*(1), 145–155. https://doi.org/10.1007/BF00153151

Tian, H., and Chen, N. H. (2018). Multi-episode chromospheric evaporation observed in a solar flare. *Astrophys. J.*, *856*(1), 34. https://doi.org/10.3847/1538-4357/aab15a

Young, P. R., Doschek, G. A., Warren, H. P., and Hara, H. (2013). Properties of a solar flare kernel observed by *Hinode* and *SDO*. *Astrophys. J.*, *766*(2), 127. https://doi.org/10.1088/0004-637X/766/2/127

Zhang, K. (2023). A novel geomagnetic satellite constellation: Science and applications. *Earth Planet. Phys.*, *7*(1), 4–21. https://doi.org/10.26464/epp2023019

Zuo, F. C., Shi, Y. Q., Chen, J. W., Zhang, X. P., Fu, W. C., Chang, Y., Gai, F. Q., Liu, S. Y., Xiong, Y., … Zhang, K. (2024). Design and technology review of the solar X-ray detector onboard the Macao Science Satellite-1B. *Sci. China E: Tech. Sci.*, *67*(11), 3365–3380. https://doi.org/10.1007/s11431-023-2699-0